Aerodynamic Characteristics Around a Generic Train Moving on Different Embankments under the Influence of Crosswind

Open Access

Izuan Amin Ishak[1,*], Mohamed Sukri Mat Ali[2], Fadhilah Mohd Sakri[3], Fathul Hakim Zulkifli[1], Nofrizalidris Darlis[1], Rahmah Mahmudin[1], Shaiful Fadzil Zainal Abidin[1], Muhamad Asri Azizul[1], Syabillah Sulaiman[1], Nor Afzanizam Samiran[1], Amir Khalid[1]

[1] Automotive and Combustion Synergies Technology Group, Advanced Technology Centre (ATC), Faculty of Engineering Technology (Mechanical), Universiti Tun Hussein Onn Malaysia, EDU Hub Pagoh, 84600 Johor, Malaysia
[2] Malaysia Japan International Institute of Technology, Universiti Teknologi Malaysia, 54100 Kuala Lumpur, Malaysia
[3] Universiti Kuala Lumpur – Malaysia Institute of Aviation Technology, Jalan Jenderam Hulu, Kampung Jenderam Hulu, 43900 Sepang, Selangor, Malaysia

ARTICLE INFO

ABSTRACT

In this article, simulations of crosswinds over a generic train model that are moving on different embankment configurations are discussed. The different configurations of embankment cases were studied using various slope inclinations (i.e. 150°, 160° and 170°). The result is also compared with the base case i.e. train running on a flat ground (FGC). The incident flow angle is varied from 0˚ to 90˚. The flow around the train has been considered incompressible and is obtained by solving the incompressible form of the Reynolds Navier-Stokes (RANS) equations combined with the SST $k - \omega$ turbulence model. A grid convergence study is presented in order to examine the reliance of the flow solution on spatial discretization. The Reynolds number used, based on the height of the train and the freestream velocity, is 3.7×10^5. In the result, it is established that variations of incident flow angle resulted in the development of different flow behaviors. Two unique flow regimes appear which represent a slender body behavior at a smaller range of incident flow angles (below 45°) and bluff body behavior at a much higher range of incident flow angles (above 45°). Due to the existence of embankment structure underneath, flow rising over the top accelerated considerably at the windward area. The wake size especially in the bluff body flow regime (above 45°) was much larger since the changes of the altitude with the flat ground allowed the wake to rotate and move more freely in the leeward region. Subsequently, changing in flow patterns has its impact on the important aerodynamic loads such as the coefficients of side force, lift force, and rolling moment in which there were also worsen for the train running on the embankment as compare to FGC.

Keywords:
Generic Train; Grid Convergence Index; Crosswind; Flow Regime; Flow Structure

---

* Corresponding author.
E-mail address: izuan@uthm.edu.my (Izuan Amin Ishak)

Penerbit
Akademia Baru

1. Introduction

Trains are an increasingly important means of transportation. Rapid developments of the train system, especially in Europe as well as Japan and some other countries have gained worldwide attention. Aggressive improvement especially in the context of train technological expansion shows a trend towards improving the travel speed and energy efficiency in the last three decades. This has sparked interest among commuters and travelers. There are numerous advantages of trains in terms of delivery as well as economic and environmental aspects. Thus, they have become one of the popular options amongst passengers for both short and long-haul travels. Therefore, it is vital for the safety aspects of the train operation to be studied more implicitly specially to cater to the demand of the faster moving train vehicle nowadays.

Crosswind is a problematic factor for the stability of a ground vehicle. Today, most types of ground transportation other than rail vehicles, such as buses, trucks, and cars, are also subject to crosswind disturbances. In the scope of rail transport, alertness on safety factors especially the vehicle's crosswind stability has grown significantly in the community. Additionally, it has become an alarming sign, especially in countries with the high speed train (HST) networks [1].

Since the vehicle's stability due to crosswind presents a safety issue, detailed information about the physics of flow behavior around the vehicle in a crosswind is desirable. Plenty of studies have to be carried out in order to evaluate the crosswind stability of a train vehicle. The fact that there are few serious incidents occurred in recent years where strong winds are thought to be the main cause of derailment intensify the importance of further research on the subject [2,3]. In the past, more than 30 wind-induced accidents of railway vehicles were reported around the world (e.g. Japan, Belgium, Italy, Switzerland, and China) [3–5]. These are the reasons that make it vital to study the crosswind stability of the railway vehicles that are certainly influenced by wind conditions.

In addition, the study of a crosswind in which the wind above the track will be particularly high is also vital [3,6,7]. Due to unavoidable geographical surface, there are some circumstances whereby the railings need to be raised above the ground. Additional infrastructures such as embankments or bridges are an alternative passage to provide a platform for the rail vehicle operation. Since the level of the railway is raised at higher altitude, the aerodynamic stability of the vehicle will be worsened. High embankments contribute a great deal to the accumulated risk of violating mechanical safety [4,5]. Aerodynamic forces tend to increase significantly for trains running on the infrastructure, which may cause in a greater likelihood of trains derailing and overturning [5,6,8,9].

To date, not a lot of investigation has been done regarding the effects of infrastructures on the train aerodynamics. The existing findings are however mostly gathered from experimental analysis [9–11]. Suzuki *et al.,* [9] performed an experimental study and examined the effects of various infrastructure configurations such as different cases of bridge girder's thickness and embankment's height. Their results show that by increasing both the thickness of the bridge girder and embankment's height, the aerodynamic side force coefficient will be increased. Despite of that, Cheli *et al.,* [10] and Bocciolone *et al.,* [11] carried out experiment studies for the same purposes i.e. the investigation of the Technical Specification for Interoperability (TSI) infrastructure scenario based on the crosswind actions on a train. As a result, Bocciolone *et al.,* [11] found that at small yaw angles, both side force and lift force coefficients are slightly higher for the embankment configuration compared to the ones measured on viaducts. This is owing to the different wind velocities at the top of the infrastructures. At low crosswind yaw angles, the embankment configuration causes flow acceleration and overpressure on the train whilst for larger yaw angles, the viaduct configuration seems to be more critical in terms of both the side and lift force coefficients [11].

In conclusion, aerodynamic aspects are considered as one of the most essential criteria that need to be tackled immensely. However, to focus on the design of the vehicle is insufficient especially since there are also other external problems particularly those associated with the crosswind and different platform conditions, both of which make the aerodynamic phenomena become more interesting to be discovered. It is anticipated that by tackling these related aerodynamic issues, safety conditions of the train operation may be guaranteed. In this study, the objective lies in the analysis of aerodynamic characteristics which include both aerodynamic load and physic flow structure and how the results reflect on the occurrence of two flow regimes (i.e. slender body flow regime and bluff body flow regime).

This paper has been organized in the following way. In Section 2, the theoretical background of aerodynamic loads and crosswind condition is described. Section 3 discusses the computational set-up inclusive the detailed model (train and its infrastructures), domain description, boundary condition and solution methodology. Section 4 prevails the grid convergence study which is done by a systematic method using the Grid Convergence Index (GCI) and the Richardson Extrapolation. Comparison of the result with previous works is also performed. Next, Section 5 discusses the outcome of the results from the present study. This include (a) the aerodynamic loads (b) the physic of flow structure and (c) the wake size in which all cases are deliberated comprehensively. Finally, the conclusion is stated in the last section of the article. Lastly, Section 6 provides the conclusions.

2. Theoretical Background

2.1 Aerodynamic Loads

A train experiences aerodynamic loads due to the normal and tangential stresses over its surface when it cruises in a crosswind. The important aerodynamic forces in regards to safety vehicle operation include the side forces (F_s) that push the vehicle sideways and the lift force (F_l) that acts upwards (tendency of the vehicle being raised up from the ground). The corresponding moments from the side force include the rolling (R_{RL}) is also considered in this study. When integrated, these stresses give rise to the resultant load components, which are usually expressed in non-dimensional form by means of force and moment coefficients. These non-dimensional parameters are chosen so that comparison can be made regardless of the train's shapes, sizes or driving speed. These parameters are expressed in Eq. (1) and graphically presented in Figure 1.
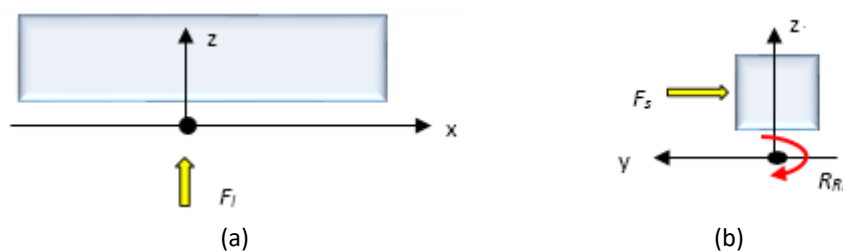

Fig. 1. Different aerodynamic loads acting on the train under the influence of a crosswind. (a) Side view (b) Front view

$$C_s = \frac{F_s}{\left(\frac{1}{2}\rho u^2 A\right)} \ , C_l = \frac{F_l}{\left(\frac{1}{2}\rho u^2 A\right)} \ , C_{RL} = \frac{R_{RL}}{\left(\frac{1}{2}\rho u^2 AH\right)} \tag{1}$$

where ρ is the density of air, u is the wind velocity relative to the vehicle, A is the projected surface area in the x-direction, and H is the height of the train body.

2.2 Crosswind

The magnitude of the aerodynamic loads of a train is influenced by the direction of the effective crosswind. Here, the effective crosswind (U_R) is defined as the vector summation between the train speeds (U_t) and the wind velocity (U_w) as shown in Figure 2.
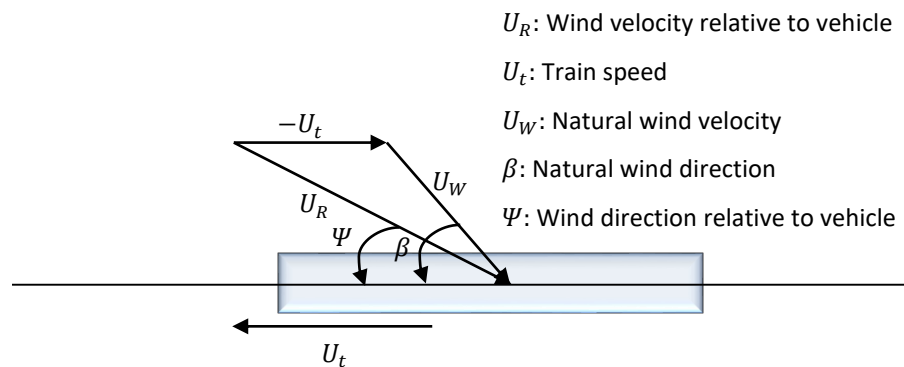
U_R: Wind velocity relative to vehicle

U_t: Train speed

U_W: Natural wind velocity

β: Natural wind direction

Ψ: Wind direction relative to vehicle

Fig. 2. Natural wind velocity relative to vehicle

3. Computational Set-up

3.1 Train Model Description

This specific model geometry is chosen as it has been used by previous investigators (experimentally by Sakuma *et al.,* [12–15] and numerically by Osth *et al.,* [16]) to represent a simplified train model. The leading side and top edges on the front are rounded using an elliptical profile with major axis in the ellipse length of $0.07H$ and the minor axis length of $0.04H$ as can be seen in Figure 3(a) to (b). The side and top edges of the rear end of the vehicle are rounded with a circular radius $0.107H$ as can be seen in Figure 3(c). Both front and rear bottom edges are not rounded and thus sharp. The length of the train is $7H$ while the width and height are both equal to H. ($W = H = 0.56$m).
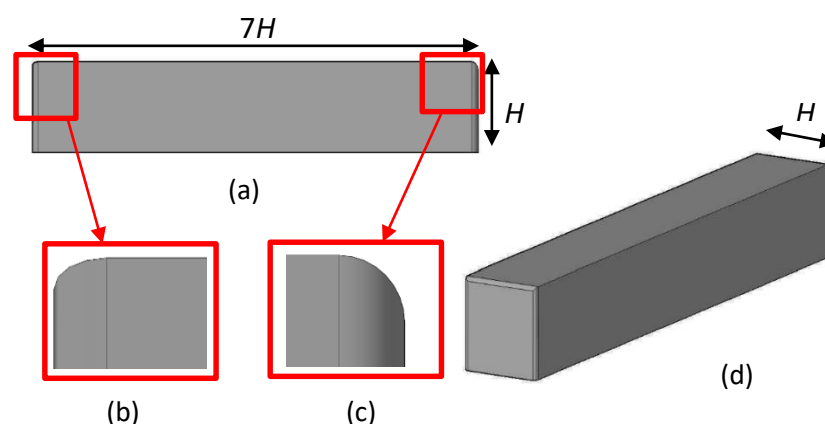
Fig. 3. Geometry of the train model with blunt nose shape. (a) Side view (b) Close view of front corner with an elliptic rounding (c) Close view of rear corner with a circular rounding (d) Isometric view

3.2 Embankment Description

The test cases can be divided into two major categories of surfaces on which the generic train model is travelling: flat ground (FGC), and embankment. Figure 4 shows the vehicle on top of an embankment. The crosswind U_∞ affects the aerodynamic properties of the train differently when the slope of the embankment, θ is varied [6,9,17]. Three slope angles are investigated in this study, i.e. θ = 150°, θ = 160° and θ = 170°. The height of the embankment is fixed at 6 meters which is based on the Technical Specifications for Interoperability (TSI) infrastructure scenario [9–11].
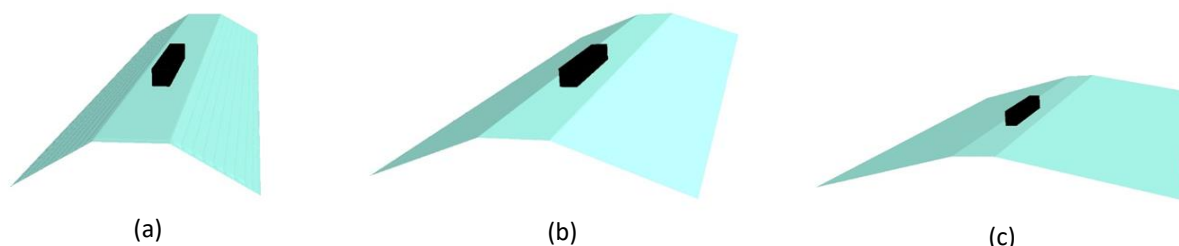

| (a) | (b) | (c) |

Fig. 4. Shapes of the embankments at three slope angles (a) 150° (b) 160° (c) 170°

3.3 Computational Domain

General guidelines on the distances between (i) the inlet and the vehicle and (ii) the vehicle and the outlet for the validation case are based on the previous investigations [13,14,18-21] i.e. distance from the inlet to the train model is 8*H* and distance from the train model to the outlet is 21*H*. Based on former research on the simulation of flows around a generic train model, these specific lengths are found to be adequate to make sure that the domain is at its optimum size and can also be considered large enough to ensure that the velocity and pressure fields are uniform at the inlet. This means that there will not be any interruption in the flow structure development across the domain area.

The generic train model is placed 0.15*H* above the ground in order to imitate the typical real train condition [22,23]. The placement of the train's model is also sufficiently far from the top and side walls (i.e. 10*H*) in order to minimize the near wall effects. Figure 5 visualized the domain for the case at 0° yaw angle. A detailed summary of the domain size change for different crosswind situations is presented in Table 1.
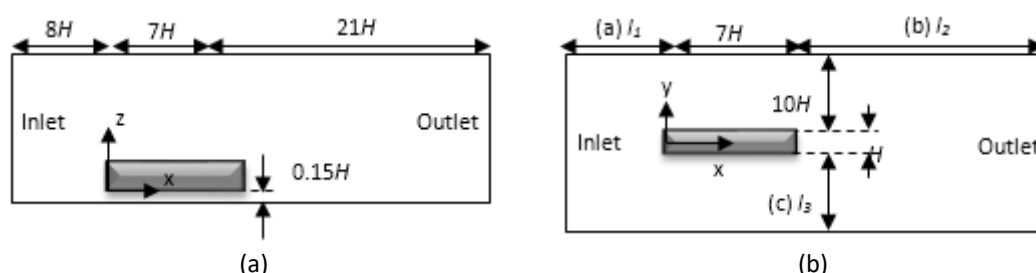

| (a) | (b) |

Fig. 5. Computational domain used in the numerical investigation for 0° yaw angle condition.
(a) Side view (b) Front view (c) Top view (Sketch only and not following the actual scale)

Table 1
Domain size parameter based on Figure
5(b) for different cases of crosswind yaw
angles

Yaw Angle (Ψ)	l_1	l_2	l_3
0°	8H	21H	10H
15°	8.4H	20.3H	10.5H
30°	8.8H	18.2H	12.8H
45°	9.2H	14.9H	16.1H
60°	9.6H	10.5H	20.5H
75°	10H	10H	21H
90°	10H	10H	21H

3.4 Boundary Condition

Visualizations of the boundary conditions are shown in Figure 6. The details of boundary conditions are explained as follows.

(a) ***Inlet:*** Uniform velocity, which represents the free stream velocity (U_∞) is applied in the *x*-direction. For crosswind conditions ($\Psi > 0°$), the resultant wind velocity will follow the component velocity vector based on the effective crosswind.

(b) ***Ground plane:*** The boundary type of moving wall is applied with the velocity component in the *x*-direction equal to the inlet velocity (U_∞) in order to prevent the development of boundary layer on the ground plane. This is also to replicate the relative movement between the train and the ground.

(c) ***Outlet:*** The homogenous Neumann boundary condition is applied at the outlet, meaning that the pressure gradient is equal to zero. This allows the flow pass through the outlet without affecting the upstream flow, provided that the upstream distance to the vehicle's body is large enough.

(d) ***Lateral side and roof plane:*** The patch type boundary condition with a freestream value similar to the inlet is used. For crosswind conditions ($\Psi > 0°$), the right plane will become an inlet whilst the left plane will be transformed to outlet boundary condition.

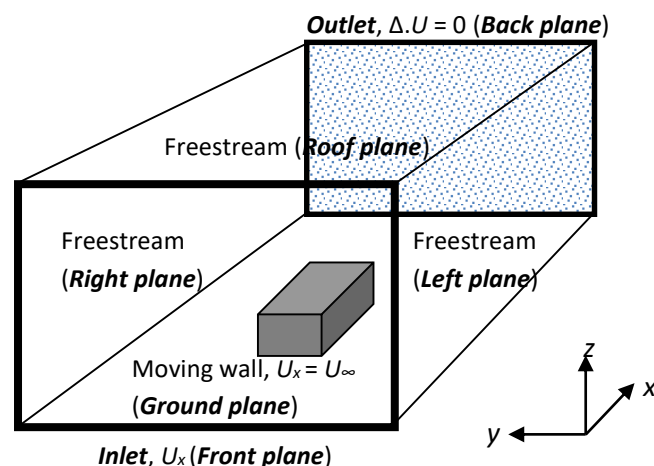(e) ***Train model surface:*** The no-slip condition is used.

Fig. 6. Boundary conditions used in the numerical investigation (not following the actual scale)

3.5 Solution Methodology

The flow around the train has been considered incompressible and is obtained by solving the incompressible form of the Reynolds Averaged Navier-Stokes (RANS) equations. The two equations which are Continuity and Navier-Stokes equations for the incompressible flow as follows.

$$\frac{\partial U_i}{\partial x_i} = 0 \tag{2}$$

$$\frac{\partial U_i}{\partial t} + U_j \frac{\partial U_i}{\partial x_j} = -\frac{1}{\rho}\frac{\partial P_i}{\partial x_i} + \frac{\partial}{\partial x_j}\left(\mu \frac{\partial U_i}{\partial x_j} - \rho \overline{u_i' u_j'}\right) \tag{3}$$

in which indices *i, j* =1, 2, 3 refer to the streamwise –*x*, cross-stream –*y* and –*z* direction in a Cartesian-coordinate system respectively. U_i and P_i are the time averaged terms, while u_i' and u_j' is the fluctuation terms of velocity.

The OpenFOAM CFD software package is used to solve these governing equations. Detail numerical settings applied throughout all case study is presented as in Table 2.

Table 2
Numerical methods used in OpenFOAM

Discretization		Scheme	Description
Time		*steadyState*	-
Spatial	Gradient	Central differencing	2nd order central differencing
	Divergence	QUICKV	3rd order
	Laplacian	Gauss linear differencing scheme	2nd order unbounded
Pressure-velocity coupling		SIMPLE	Used as steady flow algorithm
Turbulence models	RANS	$k - \omega$	Shear-Stress-Transport (SST)
Wall functions	k	*kqRWallFunction*	Acts as a zero-gradient condition for modelled k
	ω	*omegaWallFunction*	Automatic wall functions condition for ω
	ν_t	*nutkWallFunction*	Generates near-wall profile for ν_t based on modelled k

4. Validation Study
4.1 Grid Convergence Study

Solutions to three different grid refinements which represent fine, medium, and coarse grids are simulated with the aim of investigating the effect of grid dependency [13,24-28]. These different grid resolutions are carefully chosen based on grid refinement ratio (r) as shown in Table 3. Shown in Figure 7 is the detail mesh for the fine grid resolution. The train model displayed below acquire a pillar support for the purpose of comparison study with previous analysis on the same train model by Sakuma *et al.,* [12] and Osth *et al.,* [16].

Table 3
Grid parameter for case A, B and C where subscripts 1, 2 and 3 represents case A, B and C respectively

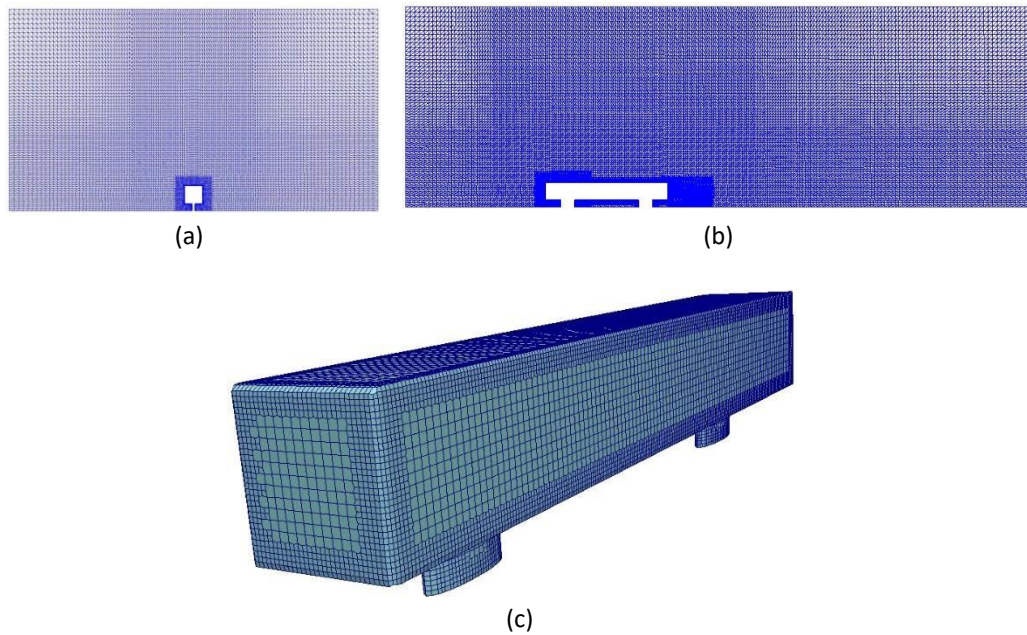| CASE	A (Fine)	B (Medium)	C (Coarse)
Total No. of Cells, N	2,114,715	951,838	359,838
Average cell size, h_{ave} (m)	0.0895	0.1168	0.1615
Average y^+	81.76	83.28	113.59
Refinement ratio, r	$r_{21} = 1.31$		$r_{32} = 1.38$

Fig. 7. Detail of mesh for the fine grid resolution. (a) at 1H from front nose cross-section (b) at middle plane cross-section, and (c) on the train model

Based on Celik *et al.,* [29], it is necessary that the ratio be at least greater than 1.3. Since the meshes are not uniform, the grid refinement ratio is calculated based on average grid size(h_{ave}). The grid refinement ratio (r) and the average cell size (h_{ave}) can be calculated as follows.

$$r_{21} = \frac{h_2}{h_1} \tag{4}$$

$$r_{32} = \frac{h_3}{h_2} \tag{5}$$

$$h_{ave} = \left[\frac{1}{N}\sum_{i=1}^{N}(\Delta V_i)\right]^{\frac{1}{3}} \tag{6}$$

where ΔV_i is the volume of the ith cell, and N is the total number of cells used for the computations.

The grid convergence study is assessed using the Richardson Extrapolation (f_{RE}) and Grid Convergence Index (GCI). By definition, the value estimated from the Richardson Extrapolation (f_{RE}) is the value that would result if the cell grid size tended to zero$(h \to 0)$. Alternatively, the GCI value indicates that the percentage of the computed value is away from the value of the asymptotic numerical value. It shows an error band on how far the solution is from the asymptotic value and how much the solution would change with a further refinement of the grid. This is accomplished by comparing GCI results of various parameters between different levels of mesh resolutions. Both of these indicators are essential in accessing a grid convergence study [13,24].

Based on the results, monotonic convergence criteria (R) are achieved since 0 < R < 1 (refer to Table 4). This can be seen clearly from Figure 8 which indicates how the value of the chosen parameter progressively moved in a converging pattern towards the Richardson extrapolated value. This also explained that the error, due to grid convergence, gradually decreased and the fine grid resolution (GCI$_{21}$) had a value of less than 1% for almost all the compared parameters (refer Table 4). To put it briefly, as the GCI reduction from the coarser grid (GCI$_{32}$) to the finer grid (GCI$_{21}$) is relatively

high, it can be said that the grid independent solution is nearly achieved, which concludes that further refinement of the grid will not greatly impact the results of flow simulation [24].
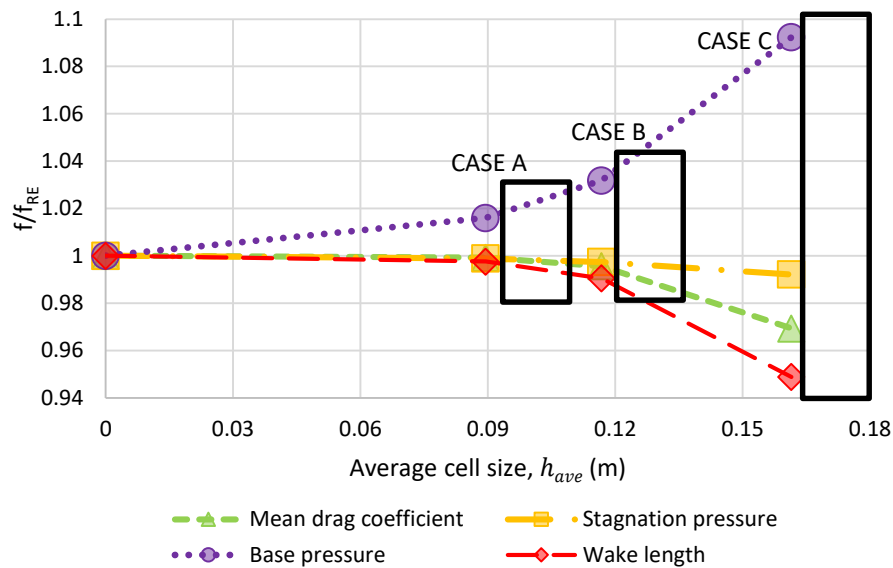

Fig. 8. Comparison of different integral parameters normalized by the extrapolated, between three grid solutions and Richardson extrapolation estimation

Table 4
Grid Convergence Index (GCI) for different parameters

CASE	$|\varepsilon_{32}|$ (10^{-2})	$|\varepsilon_{21}|(10^{-2})$	R	GCI$_{32}$ (%)	GCI$_{21}$ (%)
C_d mean	1.91	0.26	0.133	0.5542	0.1122
Stagnation Pressure ($\frac{P}{\rho u_\infty^2}$)	0.26	0.08	0.2932	0.3262	0.1307
Base Pressure (10^{-3}) ($\frac{P}{\rho u_\infty^2}$)	0.0242	0.0062	0.255	2.9056	1.0496
Wake Length (m)	2.4068	0.4101	0.170	1.1946	0.2969

4.2 Comparison with Previous Result

For validation and comparison purposes, results obtained using different turbulence models are compared with the published experimental data of Sakuma *et al.,* [12] and numerical data of Osth *et al.*, [16]. In this section, mesh used in Case A (Fine mesh) is adopted.

4.2.1 Pressure coefficient

Firstly, the pressure coefficient is selected and defined as

$$C_p = (p - p_\infty/0.5\rho U_\infty^2) \tag{7}$$

where *p* is the local static pressure and p_∞ is the free stream static pressure.

The pressure coefficient along the centreline of the train model for the case study using different turbulence model is shown in Figure 9. In general, the pressure follows the same pattern as the results of Sakuma *et al.,* [12] and Osth *et al.,* [16]. However, discrepancies occurred at the separated flow region (*s/H* = 1) on the front-roof area of the train. Recent work using various turbulence model

seems to underestimate and overestimate the negative pressure at this specific point. Following this, in some cases, the flow reattached much earlier while others reattached further downstream compared to the previous results. However, a significant similarity was observed in the reattachment region as the flow passes through the roof. In the wake region, the recent simulation slightly underestimates the pressure coefficient value, but captures the lowest peak value of pressure coefficient similar to that of Osth *et al.,* [16].
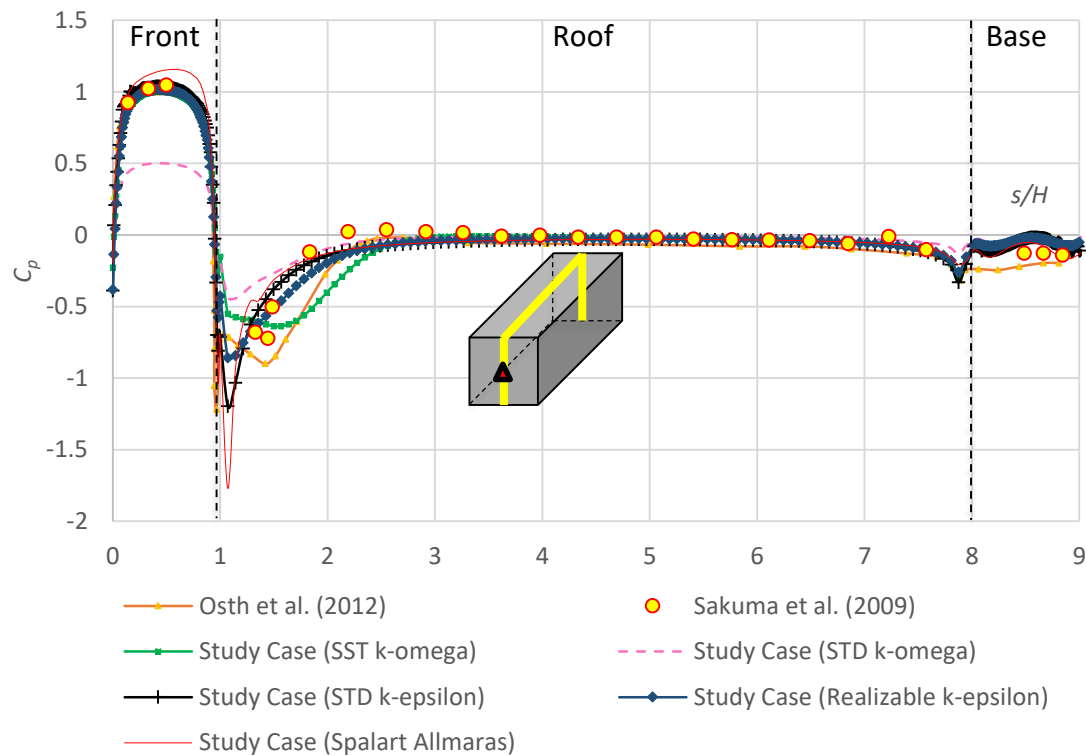

Fig. 9. Pressure coefficient along the centre line of the train model

Specifically, the outcomes of the pressure coefficient plotted along the midplane surface of the train model clearly show better results when using *SST k–ω* compared to other turbulence models. Even though the difference in the value of pressure drop is quite significant at the leading edge, the recovery of pressure towards the rest of the train's surface at the top area is more stable and nearer to the one obtained from that of Osth *et al.,* [16]. *STD k–ω* clearly underestimated the pressure especially at the front surface which is only half of the recorded value compared to others. The conventional *k–ω* turbulence model also underestimated the pressure coefficient at the separation region and at the base area. Conversely, the *STD k–ε* model provided quite convincing results, especially since it reached the same pressure drop value as that of Osth *et al.,* [16] at the separation region (s/H = 1). However, the rapid movement of the pressure recovering along the top surface of the train model makes the model doubtful to be implemented. The same situation also occurred when the *Realizable k–ε* model was implemented where the pressure recovery after a sudden drop at the leading edge did not occur as per the result of Osth *et al.,* [16]. Lastly, as expected, when the one equation model *Spalart Allmaras* was performed, its limitation on accurately computed fields that exhibited shear flow and separated flow are clearly shown in Figure 9. The figure shows the over-prediction of most pressure coefficient values. These turbulence models do not consider the diffusion and convection of turbulent energy and thus, the solution can be achieved more quickly than other types of turbulence models [30].

4.2.2 Mean drag force coefficient

The time-averaged drag force coefficient from the simulations is also compared with the ones obtained numerically by Osth *et al.,* [16] and experimentally by Sakuma *et al.,* [12]. The results are presented in Table 5. The drag coefficient is defined as follows.

$$C_d = \frac{2F_d}{\rho U_\infty^2 A_x} \tag{8}$$

where ρ is the density of air at 20°C and $A_x = H^2$.

Table 5 indicates detailed differences obtained for mean C_d when different turbulence models were applied in the simulation. The experimental results of Sakuma *et al.,* [12] and Osth *et al.,* [16] are also presented for comparison. Looking at the results, *STD k–ε* provided the results closest to that of Osth *et al.,* [16] with only a 4% difference. However, after taking into consideration the poor performance in pressure coefficient plotted in Figure 9, and with only about 6% difference in the mean drag coefficient (mean C_d) for the *SST k − ω* turbulence model, it was proved that *SST k − ω* to be more appropriate for implementation in the rest of the cases in this research. In each case simulated using various turbulence models, the under-prediction of the negative pressure in the separated region on the roof might be one of the causes of the discrepancies in the results of drag force coefficient with the previous works. This is because of the high negative pressures yielded from the separation region contributed to a decrease in the total drag coefficient of the train model. Finally, one model, *Spalart Allmaras*, showed the farthest value of the mean C_d relative to other values in comparison, suggesting that this turbulence model is not suitable for this study.

Table 5
Mean drag force coefficient (mean C_d) for comparison

Case		Mean C_d
Experiment by Sakuma *et al.*, [12]		0.86
Numerical by Osth *et al.*, [16]		0.78
Current Case	*STD k-ω*	0.71
	SST k-ω	0.73
	STD k–ε	0.75
	Realizable k–ε	0.69
	Spalart Allmaras	0.94

5. Results
5.1 Aerodynamic Loads
5.1.1 Side force

Figure 10(a) shows the effects of wind directions on the side force coefficient C_s. Similar to the baseline case i.e. the flat ground case (FGC), the change in the C_s value can be grouped into different characteristics of flow regimes. The first regime describes the slender body flow behaviour where the C_s changes almost linearly with the yaw angle i.e. at the low range of yaw angles (i.e. $\Psi \leq 45°$). In the higher range of yaw angles, the second regime (describing the bluff body flow behaviour) is observed where C_s is almost not affected by the change in the crosswind direction. It is also important to note that at the transition regime (i.e. $45° \leq \Psi \leq 60°$), the flow is in the conversion phase between slender to bluff body flow behaviour.

In general, it is obvious to notice that the C_s of a rail vehicle moving on an embankment is much higher compared to when it is moving on a FGC. For all embankment cases, the C_s graph shows an increasing trend of C_s as the yaw angle increases. For low yaw angles i.e. $\Psi \leq 15°$, the pattern of the graph follows the same as the baseline case. Then it starts to deviate at $\Psi = 30°$ where the increase in C_s becomes huge (i.e. about 107.8% increase from that of the baseline case when comparison is made with the worse embankment case). The embankment with a 160° slope leads the highest value of C_s followed by the embankment with a 170° slope and lastly, the embankment with a 150° slope. Even at $\Psi = 45°$, the value of C_s is still about 30% to 60% higher than that of the FGC. At this point, the maximum C_s of each embankment configuration is recorded. Interestingly, towards the bluff body flow regime, the value of C_s drops slightly at $\Psi = 60°$. However, as the yaw angle increases ($\Psi \geq 75°$), the value of C_s becomes more consistent, and about the same for all embankment cases but still holds about 27% higher from the baseline case.

5.1.2 Lift force

The lift force coefficient (C_l) increases to a maximum point at $\Psi = 30°$ as shown in Figure 10(b) for all embankment cases. This trend is similar with the baseline case. At this crosswind condition, the highest C_l is recorded for the embankment with 150° slope angle (i.e. about 126% increase from the baseline case). However, at $\Psi = 45°$, a steep drop in C_l happens for all embankment cases as the flow enters into the transition regime. At larger yaw angle conditions (i.e. $\Psi \geq 60°$), all of the cases exhibit similar results in which a negative C_l value is obtained.

In general, simple generalization can be perceived in the trend of C_l with yaw angle variations. In the slender body flow regime, the graph shows a fluctuating increase to a maximum value before the C_l decreases, whilst in the bluff body flow regime, the C_l value is not strongly affected by the wind direction.

5.1.3 Rolling moment

Figure 10(c) displays the comparison of the rolling moment coefficient (C_{RL}). The shape of the graph resembles the side force (C_s) graph as shown in Figure 10 (a) as the value of C_{RL} increases until it reaches an optimal value at $\Psi = 45°$. In the slender regime, the embankment with a 160° slope has the highest C_{RL}, followed by the embankment with a 170° slope and the embankment with a 150° slope. By comparison with the baseline case, the increase in value is between 23% and 41% higher. The C_{RL} then drops at $\Psi = 60°$ before it starts to be more stable. However, for the embankment with a 170º slope, the increase in value keeps continuing in the bluff body flow regime until its maximum value at $\Psi = 90°$.
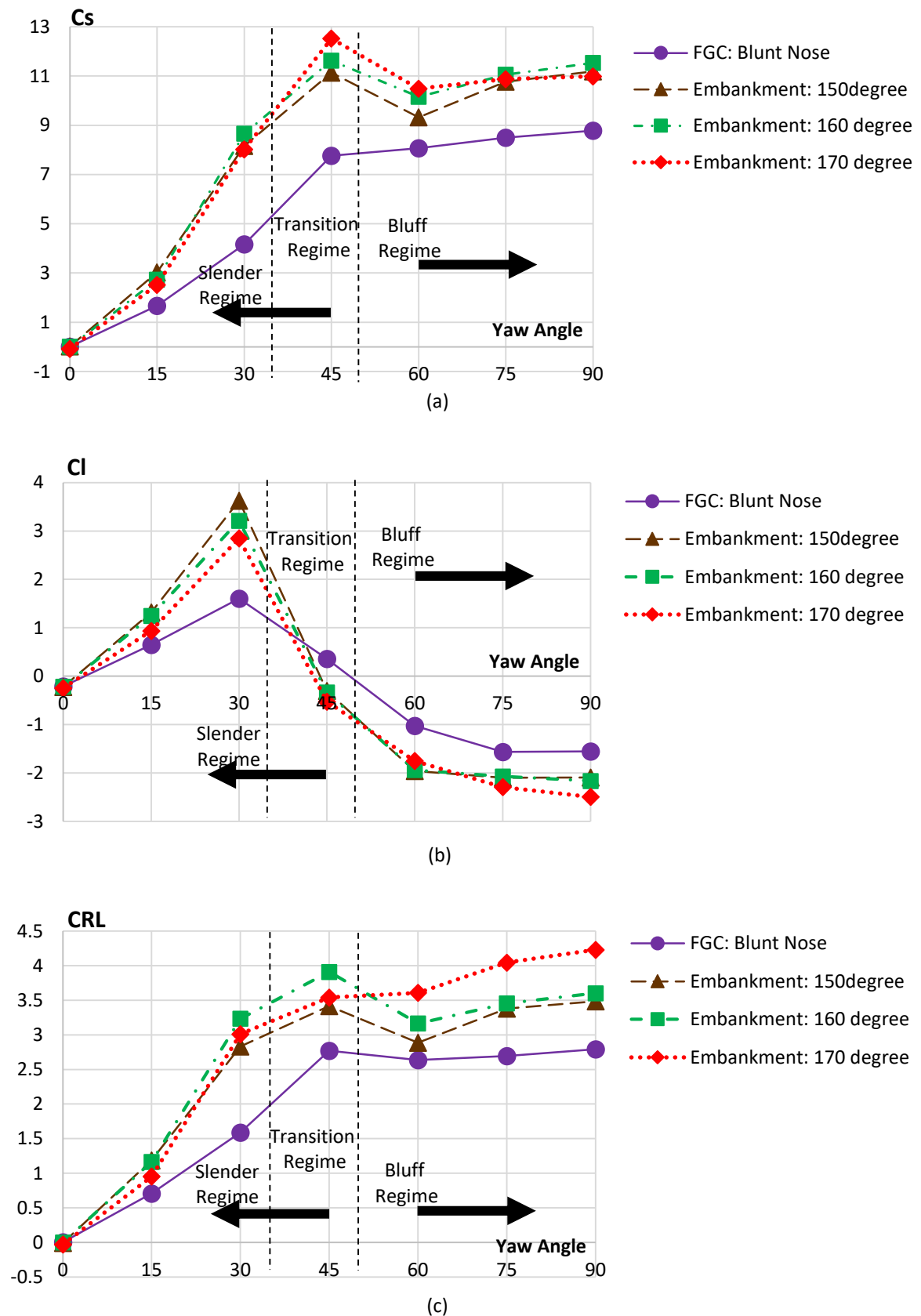
Fig. 10. Comparison of the (a) side force (C_s), (b) lift force (C_l) and (c) rolling moment (C_{RL}) with respect to different crosswind conditions for the train moving on various platforms

5.2 Streamlines of the Time-Averaged Velocity Field

In this section, the visualizations of flow structures surrounding the train area with respect to different crosswind conditions (Ψ = 0°, 30°, and 60°), are presented. Detailed flow structures are shown mostly in 2-dimensional illustrations from the side and top views. The side view is taken at x/H = 2 from the train nose whilst the top view is captured at x/H = 1/2 from the train's bottom surface. The visualizations of the flow structures are separated into two flow regimes as discussed earlier (i.e. slender body flow regime i.e. Ψ = 0°, 30° and bluff body flow regime i.e. Ψ = 60°). So far, no studies have discussed the flow structures corresponding to these two flow regimes in detail, especially for the train travelling on different embankment conditions.

5.2.1 Slender body flow regime
5.2.1.1 At Ψ = 0°

As shown in Figure 11, as the free stream flow approaches the train model, the flow particularly along the central axis is forced to move away from the body. A stagnation point appears at the central point of the model which can also be seen more clearly in the cross-stream plane as shown in Figure 12(a) to (b), which is denoted as $S_{1/2}$ (half saddle-point). From Figure 12(a), starting from the stagnation point, one part of the flow is oriented towards the bottom surface and the other part is oriented towards the roof surface of the model. As shown in the figure, a high pressure region occurs at the frontal area of the nose due to the direct impact of the approaching flow. The upper part of the flow is then separated starting from the top leading edge and hence, a large reverse flow region is formed, indicating that a well-defined vortex V_1 occurs on the roof surface of the model. This reverse flow field has high velocity as shown in Figure 11 and thus produces a low pressure region surrounding the vortex formation area. Another flow that is oriented towards the bottom surface also creates a separation of flow underneath the train model, which then creates a low pressure region as shown in Figure 12(a). At the top area, the leading edge shear layer then reattaches to the roof surface of the model at x/H = 1.2. This shear layer reattachment directly influences the drag on the model [12]. Downstream of the model, two circulatory flows (bubbles) represented as V_2 and V_3 are detected, one located above the other, and they are rotated in the opposite direction. The bubble rotating in a clockwise direction, V_2, interacts with the upper region of the vertical base, while the lower bubble, V_3 which is rotating in a counter-clockwise direction covers the bottom surface. The saddle point, S_1 defines the size of the wake region, which is about x/H = 1.
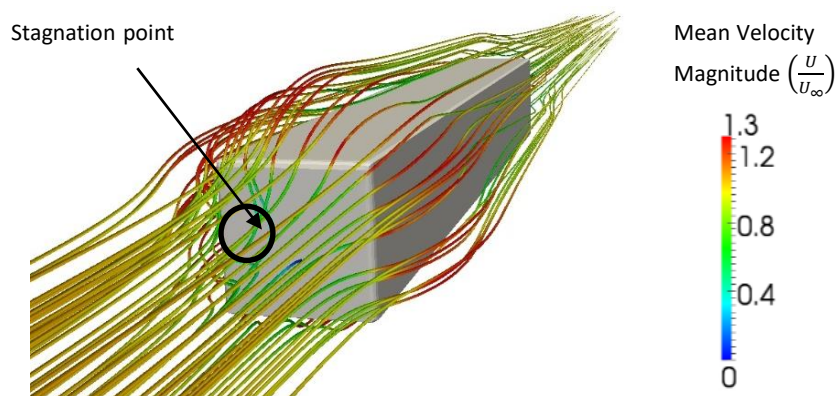

Fig. 11. Time-averaged velocity streamlines at Ψ = 0° for train travelling on the FGC

Furthermore, Figure 12(b) shows the streamlines from the horizontally symmetrical plane. The main features of the flow in this plane are two shear layers originating from the leading side edges of the model and the reversed flow region downstream of the model. As the bifurcating streamlines of the incoming flow approaches the front surface of the model, a half-saddle point of attachment, $S_{1/2}$ appears on the front surface of the model as mentioned previously. The flow parts from the vertical side edges, and forms two re-circulating flow regions and a low pressure region on both side walls of the model. This well-defined pair of vortices is denoted as V_4 and V_5. The separating and reattaching of shear layers and the recirculating flow within the separation bubbles are clearly seen from the streamline patterns. The distance of the reattachment points to the leading edge of the model is about the same as the shear layer that reattaches at the roof surface of the model (i.e. x/H = 1.2). In the wake region at the rear part of the model, a pair of similarly sized recirculation regions is identified. These two shear layers extend approximately to the same downstream location. A pair of equivalent vortices, V_6 and V_7 and a saddle point, S_2 are observed in the wake region. Again, S_2 defines the size of the wake region, which is about x/H = 1 ($S_1 \approx S_2$).
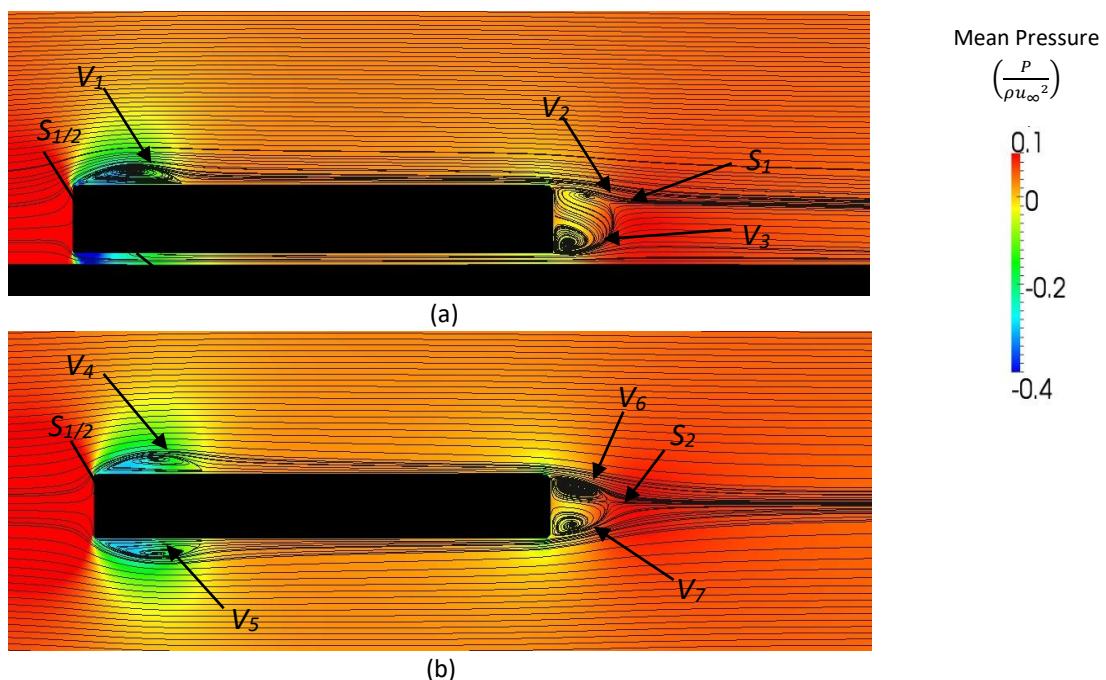

Fig. 12. Time-averaged velocity fields on the (a) side view and (b) top view of the train models

On the other hand, illustrations in Figure 13 are the free stream flows approaching the train model that is positioned on top of different embankment conditions. As can be seen, regardless of variation in shapes and configurations of the embankment, at Ψ = 0°, the flow structures surrounding the train are completely identical. The flow experiences separation along the leading edges, leading to the formation of different recirculation bubbles as presented for the train moving on the flat ground case (FGC) (refer Figure 11 and 12). It is further confirmed by the values of global properties as shown in Figure 10(a) to (c) whereby all values attained for the vehicle moving on the embankments at Ψ = 0° are exactly in parallel with the data obtained whilst the train is travelling on the FGC.
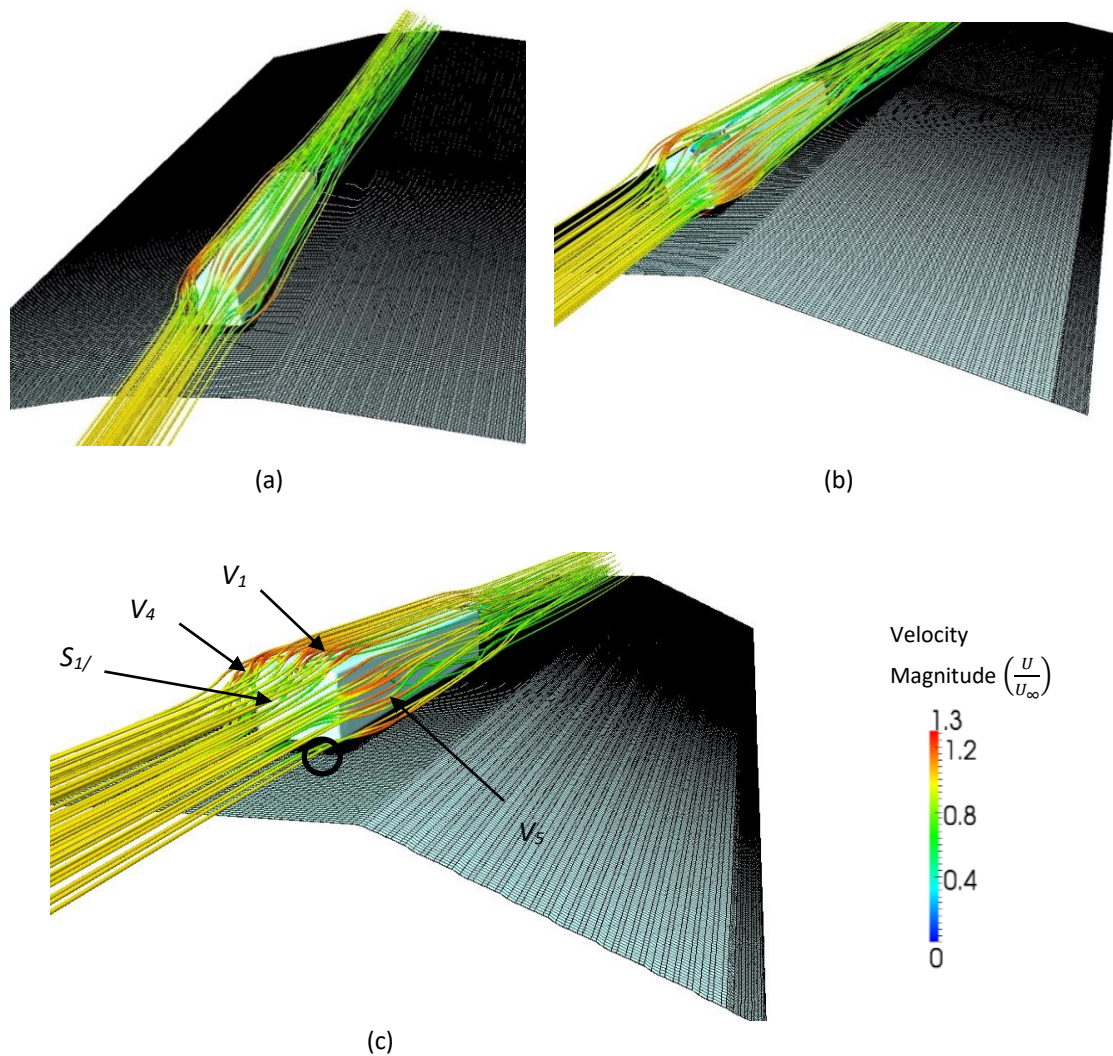
Fig. 13. Velocity streamlines passing the generic train at $\Psi = 0°$ for the embankment cases of (a) 170° embankment slope (b) 160° embankment slope (c) 150° embankment slope

5.2.1.2 At $\Psi = 30°$

The vortices especially on the top and leeward surface start to intensify and become larger at $\Psi = 30°$ for all embankment cases as shown in Figure 14(a)-(c). This correspond to the increasing of low pressure region at the separation area. It is clear that vortex $V_{(b)}$ starts to suppress vortex $V_{(1a)}$ in the case of the embankment with a 150° slope whilst for the embankment cases of 160° and 170° slopes, vortex $V_{(1a)}$ starts to shed away from the vehicle body as shown in Figure 14(b)-(c), which is also reflected in the isosurfaces of Q-criterion as shown in Figure 15. On the top separation region, the reattachment point of vortex $V_{(c)}$ is hardly seen since the size of the vortex becomes more apparent, and it starts to get infused with vortex $V_{(b)}$ on the leeward side. However, since each vortex core can still be easily seen, the flow is still acting like the slender body flow.
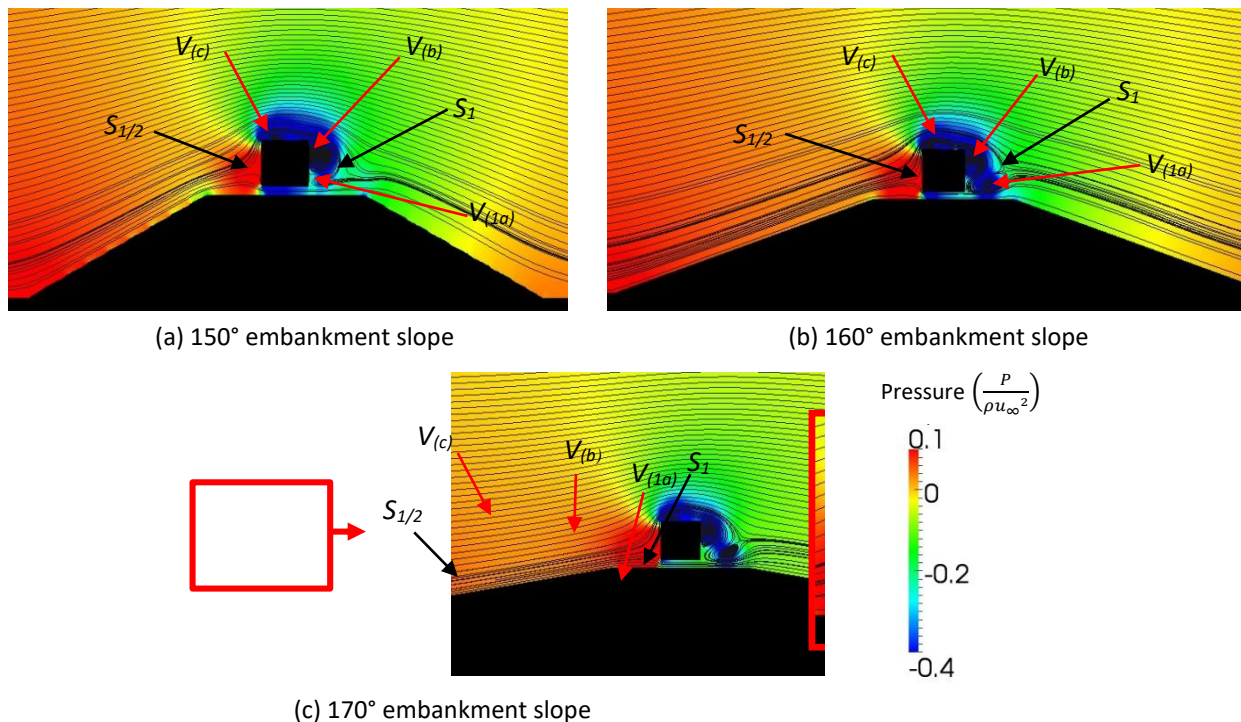
(a) 150° embankment slope

(b) 160° embankment slope

(c) 170° embankment slope

Fig. 14. Streamlines superimposed on the pressure contour for different embankment configurations at *x/H = 2* from the train's nose for *Ψ = 30°*

From the top view, the wake on the leeward area becomes obvious based on the longer area of low pressure region formed on the side surface of vehicle (see Figure 16(a) to (c)). At the trailing edge, the wakes become weaker and start to fuse with the leeward vortices. In terms of the aerodynamic loads, at *Ψ = 30°*, this crosswind condition shows the maximum lift force coefficient (C_l) as observed in Figure 10 (b). This happens because the ratio of lower pressure region on the top of the train to that of the underbody the maximum. Since the pressure at the top is considerably low, there is an upward force acting from the train underbody. Moreover, the side force (C_s) of all embankment cases at this yaw angle condition becomes even larger because of the increasing area of higher pressure region on the windward surface of the train as a result of more intense pressure acting on the windward surface of the vehicle (refer Figure 10 (a)).
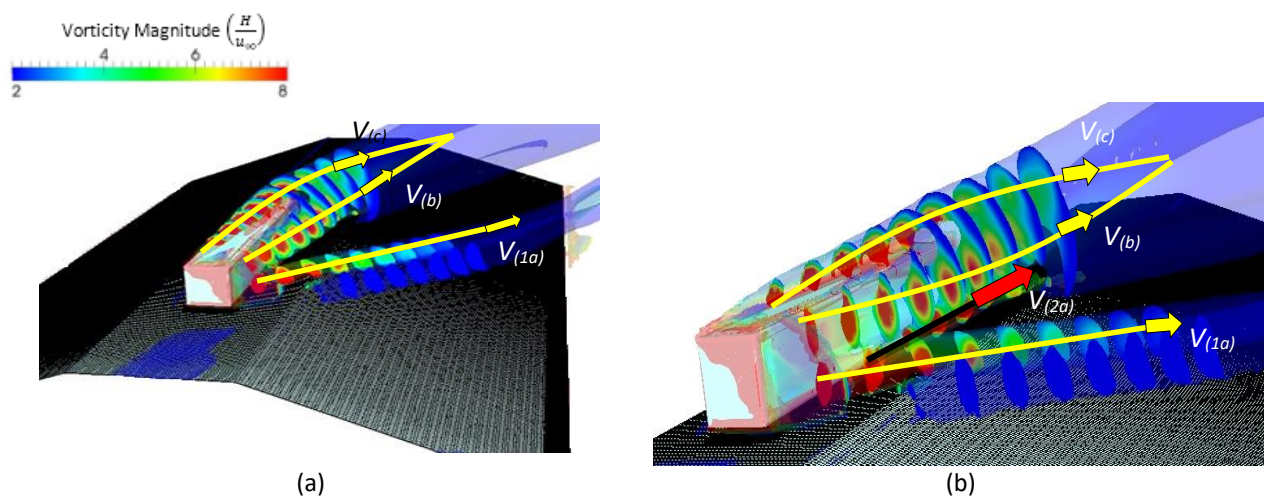

(a)

(b)

Fig. 15. Isosurfaces of *Q*-criterion for the train model with the embankment of a 160° slope at *Ψ = 30°* (a) front view (b) side view

(a) 150° embankment slope

(b) 160° embankment slope
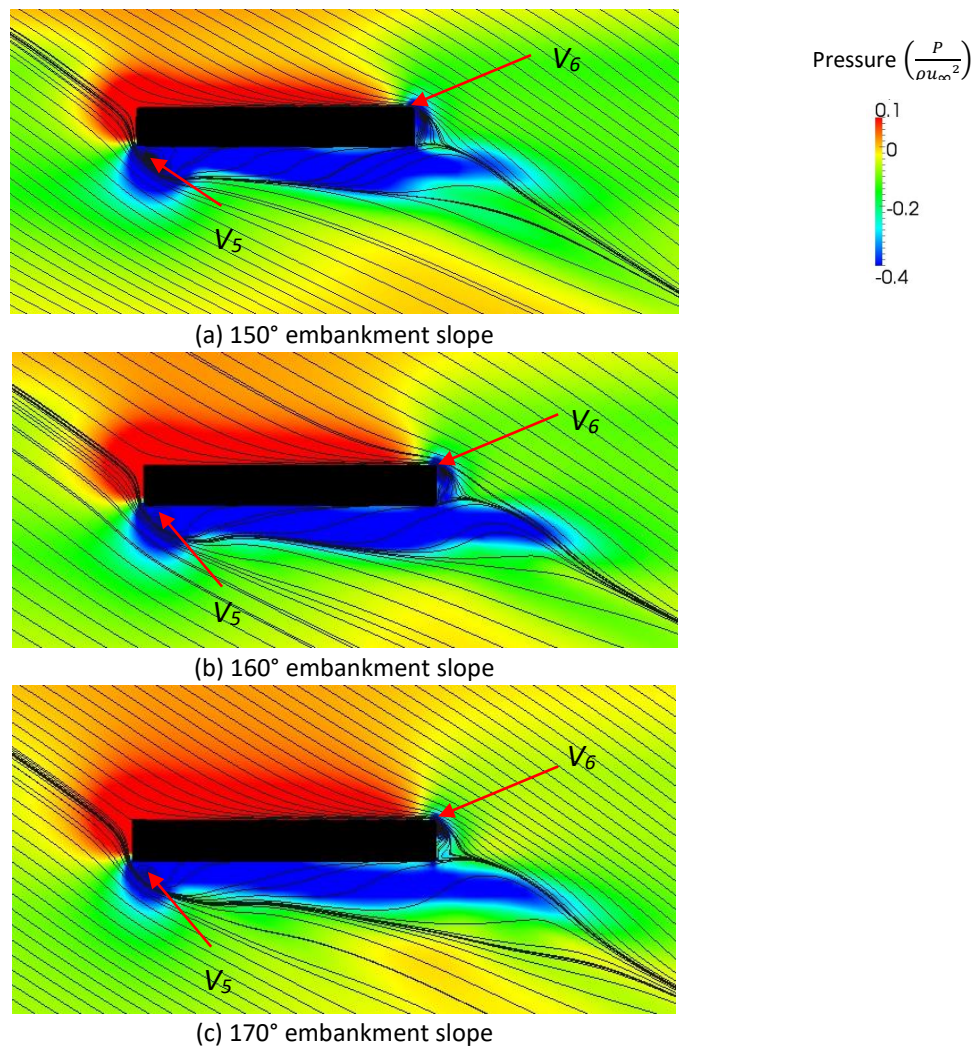
(c) 170° embankment slope

Fig. 16. Streamlines superimposed on the pressure contour for different embankment configurations at *x/H = 1/2* from the train's bottom surface (top view) for *Ψ* = 30°

5.2.2 Bluff body flow regime
5.2.2.1 At *Ψ* = 60°

At this crosswind condition*,* for all embankment cases, vortex $V_{(c)}$ has completely rolled up with vortex $V_{(b)}$ on the leeward region as shown in Figure 17(a) to (c). The merging of these vortices transforms the resulting vortex to enlarge in the leeward area. This occurrence highlights the transformation of the flow behaviour from the slender body flow regime to the bluff body flow regime. In this regime, the existence of a separated flow region in the leeward area is shown by the plot of isosurfaces of *Q*-criterion in Figure 18 for the embankment with a 160° slope. For the case of the embankment with a 150° slope, vortex $V_{(1a)}$ drifts further away in the leeward area. This has resulted in the large size of vortex produced for which the expanded wake length is more than three times (i.e. 4*H*) longer than that of the previous wind condition (i.e. when *Ψ* = 45°, refer to Table 6). However, for the embankments with a 160° slope and 170° slope, vortex $V_{(1a)}$ and vortex $V_{(2a)}$ maintain their original positions as shown in Figure 17(b) to (c). This has resulted in only a small increase in wake length that is about 1.67*H* for both embankment cases.
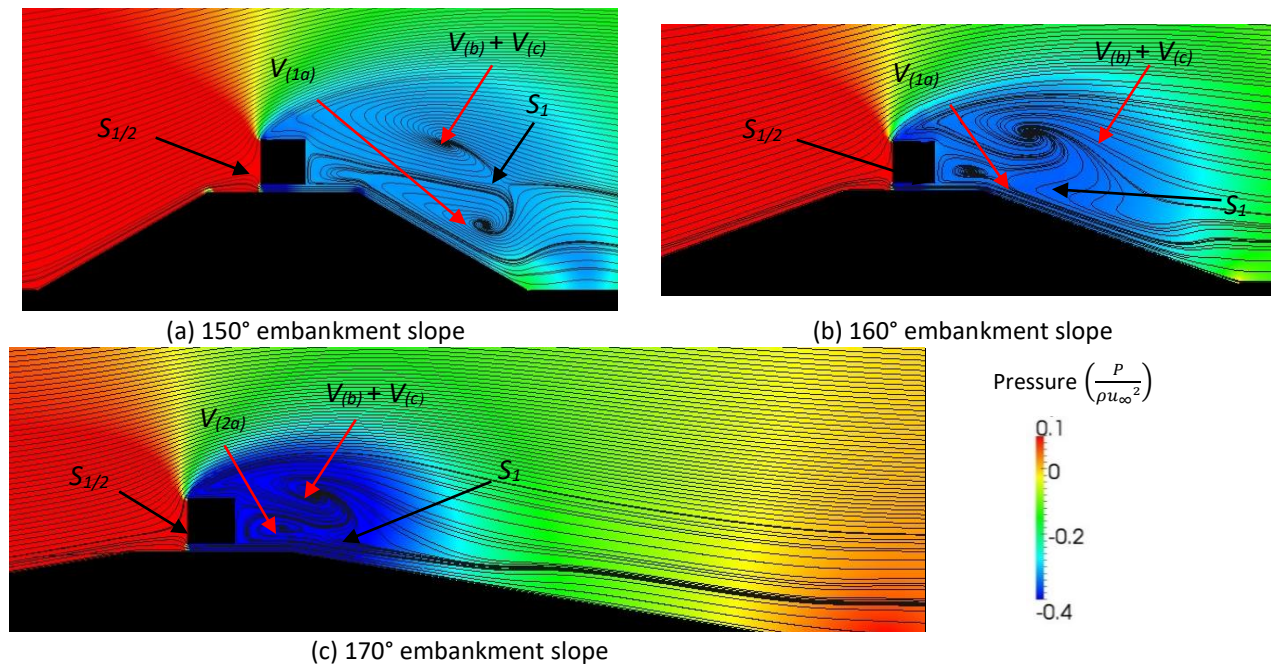
(a) 150° embankment slope

(b) 160° embankment slope

(c) 170° embankment slope

Fig. 17. Streamlines superimposed on the pressure contour for different embankment configurations at $x/H = 2$ from the train's nose for $\Psi = 60°$
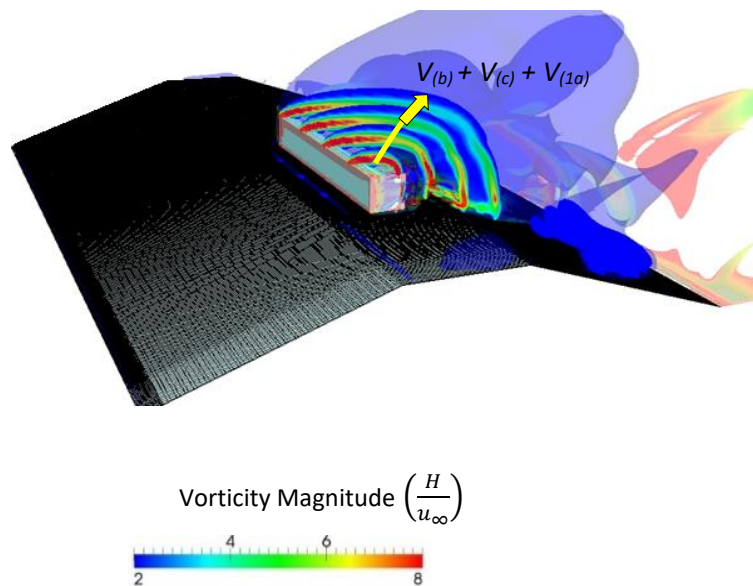

Fig. 18. Isosurfaces of Q-criterion at $\Psi = 60°$ for the train model on the top of the embankment with a 160° slope

From the top view, both vortices V_5 and V_8 start to rotate side by side in the opposite direction as can be seen in Figure 19(a) to (c). In terms of the aerodynamic loads, at this crosswind condition, C_l becomes negative as shown in Figure 10(b). This happens because vortex $V_{(c)}$ has no longer appeared above the top of the train, resulting in much higher pressure acting from the top in the downward direction.
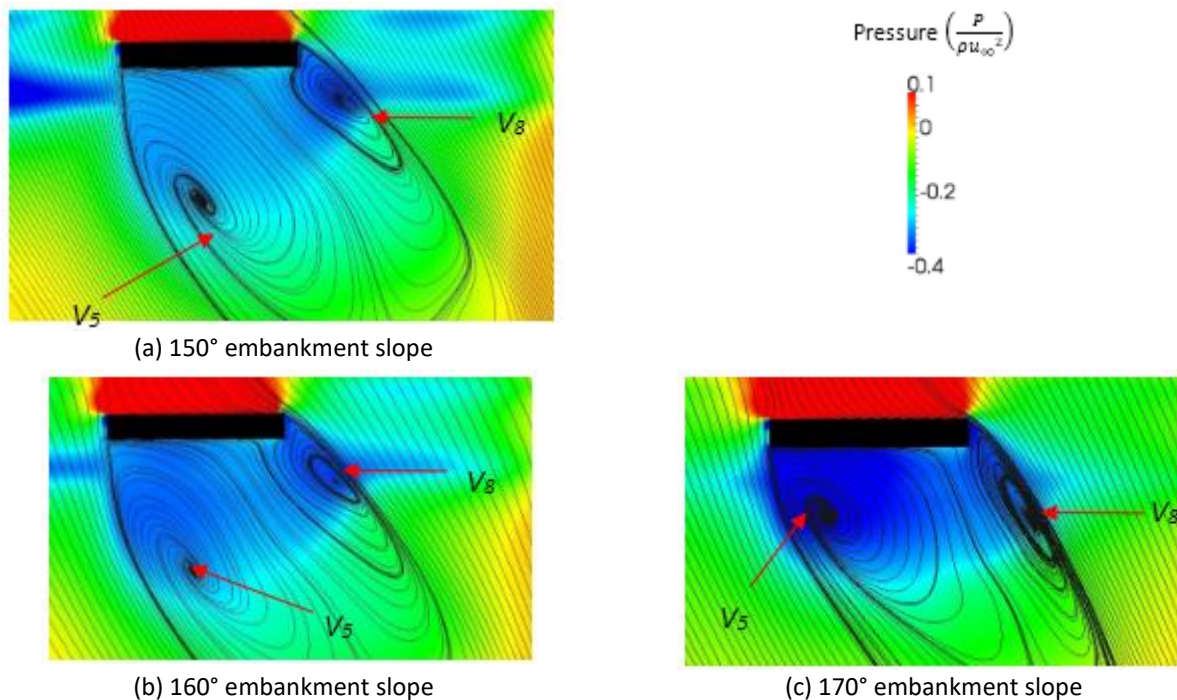
(a) 150° embankment slope

(b) 160° embankment slope

(c) 170° embankment slope

Fig. 19. Streamlines superimposed on the pressure contour for different embankment configurations at $x/H = 1/2$ from the train's bottom surface (top view) for $\Psi = 60°$

Meanwhile, the C_s value starts to drop at this crosswind condition. This is because of slight increase in the pressure in the leeward area as a result of vortex core that sheds away (see Figure 17). Hence, the balance between forces in the windward and leeward areas become less intense compared to the previous wind condition. This highlights the flow behavior that is in the transition regime towards the bluff body flow behavior.

Table 6
Measured wake sizes based on the location of the saddle point from the train's leeward surface

Case Yaw angle	Flat Ground (FGC)	Embankment slope angle = 150°	Embankment slope angle = 160°	Embankment slope angle = 170°
15°	0.77H	1H	1H	0.76H
30°	1.08H	0.67H	1H	1H
45°	1.12H	1.3H	1H	1.3H
60°	1.51H	4H	1.67H	2H
75°	2.50H	7.15H	-	7.78H
90°	4.30H	10.5H	-	17.78H

5.3 Evaluation of Wake Flow Based on Flow Regimes

Vortex shedding behind the train model provides additional information regarding the flow behaviour. Referring to Ali *et al.,* [31] and Samion *et al.,* [32], based on the position of the recirculation region, the flow behaviour in this case can be classified as the flow in a regime where the bluff body is considered to be isolated but with the effect of ground condition on one side of the surface. Moreover, based on the wake sizes formed with respect to the different wind yaw angles and ground conditions, the classification of the flow behaviour can be further categorized into two

different flow regimes as proposed in this study (i.e. slender body flow regime and bluff body flow regime).

From Figure 20, at $\Psi = 0°$, the wake size is about $x/H = 1$ for all case studies for which the results obtained are coherent with the previous studies [31,32]. The classification of the new regimes proposed in this study has extended the knowledge of wake size behind bluff bodies based on different crosswind conditions. The results show that for the slender body flow regime ($\Psi \leq 45°$), the wake length is shorter than $x/H = 2$. Conversely, in the bluff body flow regime ($\Psi \geq 60°$), the wake length is larger than $x/H = 2$. Between these two flow regimes, a transition regime exists which signifies the region where the flow behaviour starts to change. In this condition, the wake size is either smaller or distinctly larger. On top of that, it can also be seen that the wake size progression in the bluff body flow regime occurs much faster than in the slender body flow regime. For the different platform case scenarios, the rate of movement of the wake is higher for the embankment cases as compared to the FGC. This trend obviously has its impact on the aerodynamic loads as discussed earlier.
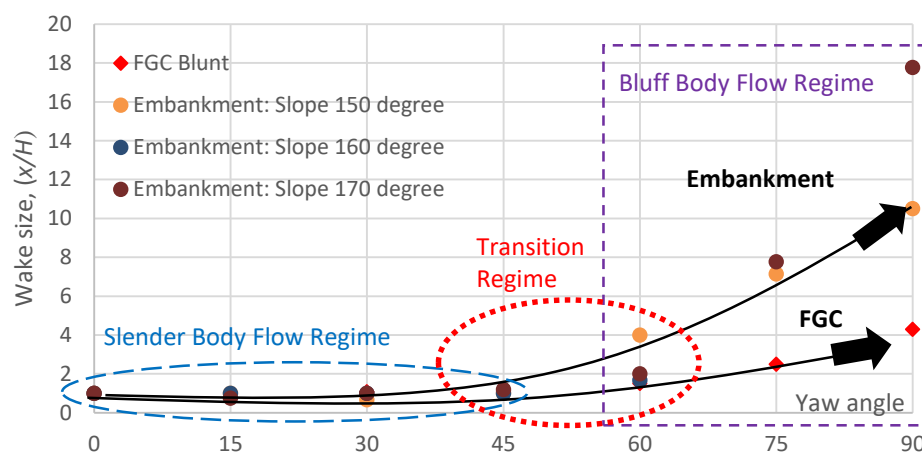

Fig. 20. Comparison of the wake sizes of different ground scenarios with respect to the different yaw angle

6. Conclusions

This paper presents the investigations on the aerodynamic charateristics inclusive of aerodynamic loads, the flow structure, and the associated global properties of a generic train model travelling on different embankment conditions under the influence of crosswind. Since the research is based on the numerical approach, a systematic validation study was conducted in making sure the accuracy of the results attained.

From the results, it was found that the aerodynamic loads are majorly influenced by both the crosswind yaw angle as well as the ground condition under which the train is travelling. Important parameters that have a major influence on the train stability including the side force (C_s), the lift force (C_l), and the rolling moment (C_{RL}) showed that the embankment cases produced the worse results of these parameters compared to the baseline (FGC). Both C_s and C_{RL} were critical at high yaw angles and reached maximum values at $\Psi = 45°$ and $\Psi = 60°$. Interestingly, the different flow regime behavior have a significant impact on these values. At slender body flow regime (i.e. $\Psi \leq 45°$), the change in the C_s and C_{RL} was almost linear with the yaw angle whilst at bluff body flow regime (i.e. $\Psi \geq 60°$), these values were less affected by the change in the crosswind yaw angles in which it shows a more consistent values.

In terms of flow structures, the main characteristic of the flow representing the slender body flow regime is the occurrence of individual vortex cores at each separation point. At this crosswind condition, it is obvious to see that all vortices were sliding near the train top and leeward surfaces. On the other hand, at the bluff body flow regime, there were an occurrence of massive separated flow regions resulted from the merging of vortices on the leeward side of the train. This, in turn, reflected on the enlargement of the vortices that became more apparent as the flow yaw angle increased. In regards to the different case scenarios (i.e. FGC and the embankments), the physics of flow structures displayed a similarity in behavior with respect to the different flow regime conditions. However, the size dissimilarities of the vortices formed can be observed when a critical examination on the flow structures was made. Eventually, this corresponded to the different wake sizes in the leeward region. For the slender regime (i.e. $\Psi \leq 45°$), the wake size of below $x/H = 2$ was expected whilst for the bluff regime (i.e. $\Psi \geq 60°$), the wake size above $x/H = 2$ was found.

In a nutshell, this research has successfully contributed to the existing knowledge in the aspect of train aerodynamics. The introduction of the embankments together with the crosswind will worsen the aerodynamic properties surround the train. Henceforth, the research objectives have been successfully achieved.

Acknowledgement

References

[1]   Raghunathan, Raghu S., H-D. Kim, and Toshiaki Setoguchi. "Aerodynamics of high-speed railway train." *Progress in Aerospace sciences* 38, no. 6-7 (2002): 469-514.

[2]   Alam, Firoz, and Simon Watkins. "Crosswinds effects on high cube freight trains." In *The third BSME-ASME thermal engineering conference* (2006): 7-12.

[3]   Zhang, XIaoyu. *Crosswind stability of vehicles under nonstationary wind excitation*. Vol. 28. KIT Scientific Publishing, 2015.

[4]   Baker, C. J. "The simulation of unsteady aerodynamic cross wind forces on trains." *Journal of wind engineering and industrial aerodynamics* 98, no. 2 (2010): 88-99.

[5]   Proppe, Carsten, and Christian Wetzel. "A probabilistic approach for assessing the crosswind stability of ground vehicles." *Vehicle system dynamics* 48, no. S1 (2010): 411-428.

[6]   Diedrichs, Ben, Mikael Sima, A. Orellano, and Henrik Tengstrand. "Crosswind stability of a high-speed train on a high embankment." *Proceedings of the Institution of Mechanical Engineers, Part F: Journal of Rail and Rapid Transit* 221, no. 2 (2007): 205-225.

[7]   Ekeroth, F., N. Kalmteg, J. Pilqvist, and J. Runsten. "Crosswind flow around a high-speed train on embankment-an experimental and numerical study." PhD diss., Master's thesis, Chalmers University of Technology, The Institution of Applied Mechanics, Division of Fluid Mechanics, Gothenburg, Sweden, 2009.

[8]   Baker, C. J. "The determination of topographical exposure factors for railway embankments." *Journal of Wind Engineering and Industrial Aerodynamics* 21, no. 1 (1985): 89-99.

[9]   Suzuki, Minoru, Katsuji Tanemoto, and Tatsuo Maeda. "Aerodynamic characteristics of train/vehicles under cross winds." *Journal of Wind Engineering and Industrial Aerodynamics* 91, no. 1-2 (2003): 209-218.

[10]   Cheli, Federico, Roberto Corradi, Daniele Rocchi, Gisella Tomasini, and Emilio Maestrini. "Wind tunnel tests on train scale models to investigate the effect of infrastructure scenario." *Journal of Wind Engineering and Industrial Aerodynamics* 98, no. 6-7 (2010): 353-362.

[11]   Bocciolone, Marco, Federico Cheli, Roberto Corradi, Sara Muggiasca, and Gisella Tomasini. "Crosswind action on rail vehicles: wind tunnel experimental analyses." *Journal of wind engineering and industrial aerodynamics* 96, no. 5 (2008): 584-610.

[12]   SAKUMA, Yutaka, and Atsushi IDO. "Wind tunnel experiments on reducing separated flow region around front ends of vehicles on meter-gauge railway lines." *Quarterly Report of RTRI* 50, no. 1 (2009): 20-25.

[13]   Ishak, Izuan Amin, Mohamed Sukri Mat Alia, and Sheikh Ahmad Zaki Shaikh Salim. "Mesh size refining for a simulation of flow around a generic train model." *Wind and Structures* 24, no. 3 (2017): 223-247.

[14]   Ishak, Izuan Amin, Mohamed Sukri Mat Ali, Mohamad Fitri Mohd Yakub, and Sheikh Ahmad Zaki Shaikh Salim.

"Effect of crosswinds on aerodynamic characteristics around a generic train model." *International Journal of Rail Transportation* 7, no. 1 (2019): 23-54.

[15] Ishak, I. A., M. S. M. Ali, and SAZ Shaikh Salim. "Numerical simulation of flow around a simplified high-speed train model using OpenFOAM." In *IOP Conference Series: Materials Science and Engineering*, vol. 152, no. 1, p. 012047. IOP Publishing, 2016.

[16] Östh, Jan, and Sinisa Krajnovic. "Simulations of flow around a simplified train model with a drag reducing device." In *Proceedings from Conference on Modelling fluid flow CMFF'12 (edited by J. Vad), September 4-7, 2012, Budapest*. 2012.

[17] Baker, C. J. "The determination of topographical exposure factors for railway embankments." *Journal of Wind Engineering and Industrial Aerodynamics* 21, no. 1 (1985): 89-99.

[18] Hemida, Hassan. *Numerical simulations of flows around trains and buses in cross winds*. Chalmers University of Technology, 2008.

[19] Krajnović, Siniša, Per Ringqvist, Koji Nakade, and Branislav Basara. "Large eddy simulation of the flow around a simplified train moving through a crosswind flow." *Journal of Wind Engineering and Industrial Aerodynamics* 110 (2012): 86-99.

[20] Hemida, Hassan, Sinisa Krajnovic, and Lars Davidson. "Large-eddy simulation of the flow around a simplified high speed train under the influence of a cross-wind." In *17th AIAA Computational Fluid Dynamics Conference*, p. 5354. 2005.

[21] CEN 14067-4, *Railway applications - aerodynamics Part 4: Requirements and test procedures for aerodynamics on open track*.

[22] Rezvani, Mohammad Ali, and Masoud Mohebbi. "Numerical calculations of aerodynamic performance for ATM train at crosswind conditions." *Wind and Structures* 18, no. 5 (2014): 529-548.

[23] Asress, Mulugeta Biadgo, and Jelena Svorcan. "Numerical investigation on the aerodynamic characteristics of high-speed train under turbulent crosswind." *Journal of Modern Transportation* 22, no. 4 (2014): 225-234.

[24] Ali, Mohamed Sukri Mat, Con J. Doolan, and Vincent Wheatley. "Grid convergence study for a two-dimensional simulation of flow around a square cylinder at a low Reynolds number." In *Seventh International Conference on CFD in The Minerals and Process Industries (ed. PJ Witt & MP Schwarz)*, pp. 1-6. 2009.

[25] N. H. Shaharuddin, M. Sukri, M. Ali, S. Mansor, and S. Muhamad. "Numerical Study For Flow Over A Realistic Generic Model , DrivAer , Using URANS." *J. Adv. Res. Fluid Mech. Therm. Sci.* 48, no. 2 (2018): 183–195.

[26] Maruai, Nurshafinaz Mohd, Mohamed Sukri Mat Ali, Mohamad Hafiz Ismail, and Sheikh Ahmad Zaki. "Flow-induced vibration of a square cylinder and downstream flat plate associated with micro-scale energy harvester." *Journal of Wind Engineering and Industrial Aerodynamics* 175 (2018): 264-282.

[27] Jehad, D G, Hashim, G A, Zarzoor, A K and Azwadi, C S Nor. "Numerical Study of Turbulent Flow over Backward Facing Step with Different Turbulence Models." *Journal of Advanced Research Design 4,* no. 1 (2015): 20-27.

[28] Yazid, A W Muhammad, Azwadi, C S Nor, Salim, S Mohamed and Mansor, S. "Preliminary Study on the Wind Flow and Pollutant Dispersion in an Idealized Street Canyon." *Journal of Advanced Research Design 1*, no. 1 (2014): 1-17.

[29] Celik, Ishmail B., Urmila Ghia, Patrick J. Roache, and Christopher J. Freitas. "Procedure for estimation and reporting of uncertainty due to discretization in CFD applications." *Journal of fluids Engineering-Transactions of the ASME* 130, no. 7 (2008).

[30] Bruno, Luca, and Giuseppe Mancini. "Importance of deck details in bridge aerodynamics." *Structural Engineering International* 12, no. 4 (2002): 289-294.

[31] Ali, Mohamed Sukri Mat, Con J. Doolan, and Vincent Wheatley. "The sound generated by a square cylinder with a splitter plate at low Reynolds number." *Journal of sound and vibration* 330, no. 15 (2011): 3620-3635.

[32] Samion, Siti Ruhliah Lizarose, Mohamed Sukri Mat Ali, Aminudin Abu, Con J. Doolan, and Ric Zong-Yang Porteous. "Aerodynamic sound from a square cylinder with a downstream wedge." *Aerospace Science and Technology* 53 (2016): 85-94.